Solid solution of zirconium on the M-site in Ti$_2$AlC MAX phase coatings: Synthesis, structure and mechanical properties

Kaihang Wang [a,b], Zhongchang Li [a,b], Yan Zhang [a], Guanshui Ma [a], Guangxue Zhou [a], Peiling Ke [a,b], Zhenyu Wang [a,*], Aiying Wang [a,b,*]

[a] *Key Laboratory of Advanced Marine Materials, Ningbo Institute of Materials Technology and Engineering, Chinese Academy of Sciences, Ningbo 315201, China*
[b] *Center of Materials Science and Optoelectronics Engineering, University of Chinese Academy of Sciences, Beijing 100049, China*

ARTICLE INFO

ABSTRACT

Ti$_2$AlC MAX phase is considered an ideal candidate for surface protective coatings in harsh environments due to its excellent resistance to oxidation and corrosion, yet poor mechanical properties are a key bottleneck for practical applications. In this work, taking the conception of solid solution, high-purity and high-hardness (Ti, Zr)$_2$AlC coatings were synthesized on Ti-6Al-4V substrates using a multiple-target magnetron sputtering technique combined with subsequent annealing. The as-deposited Ti-Zr-Al-C coating was partially crystalline containing TiAl$_x$ phase, and MAX phases formed after annealing at 750 °C for 90 min. Comprehensive X-ray diffraction and high-resolution TEM analysis identified the formation of solid solution (Ti$_{0.9}$Zr$_{0.1}$)$_2$AlC. The incorporation of Zr reduced the surface roughness and grain size of the coatings due to the increased nucleation sites and the suppressed atomic diffusion. Comparing with pristine Ti$_2$AlC coating, the hardness of the (Ti$_{0.9}$Zr$_{0.1}$)$_2$AlC coating was enhanced by 30 % from 12.8 GPa to 16.6 GPa. This enhancement can be ascribed to the synergistic strengthening from solid solution and grain refinement. However, fracture toughness slightly deteriorated in the (Ti$_{0.9}$Zr$_{0.1}$)$_2$AlC coating due to the preferential crack path along the refined-grain boundaries.

1. Introduction

MAX phases are a family of nano-laminated ternary carbide and nitride ceramics with a hexagonal crystal structure, which can be described by the general formula M$_{n+1}$AX$_n$, where M is an early transition metal element, A is an A group element, and X is C or N [1]. Furthermore, MAX phases with B as the X-site element have attracted wide attention and research in recent years [2–7]. In the crystal structure of MAX phases, M$_{n+1}$X$_n$ layers and A layers are stacked along the c-axis and connected by weaker M–A bonds compared with stronger M–X bonds in M$_{n+1}$X$_n$ layers [8]. Due to their special nano-laminated structure and a combination of covalent, ionic and metallic bonds, MAX phases possess unique properties of both metals and ceramics, such as easy machinability, high stiffness, good oxidation resistance, as well as high chemical and thermal stability [9,10]. In particular, Al-containing MAX phases, such as Ti$_2$AlC, Ti$_3$AlC$_2$ and Cr$_2$AlC, can form continuous Al$_2$O$_3$ protective scales through the high-temperature diffusion of Al atoms and exhibit more remarkable oxidation

resistance than other MAX phase candidates [11–13]. Among them, Ti$_2$AlC, with its excellent self-healing ability and corrosion resistance, is an ideal candidate for protective coatings used in harsh environments like high temperature, heavy irradiation, severe corrosive media, or a combination of them [14–17]. However, compared with relevant binary carbides or nitrides, MAX phases are soft and have poor deformation resistance due to the relatively weaker M–A bonds. The Vickers hardness of bulk MAX phases is only in the range of 2–8 GPa, which is lower than most structural ceramics [16]. When subject to a heavy load, such low hardness could lead to significant deformation, most likely resulting in cracking and failure during practical operation.

Adding secondary phases to form composites and doping elements to form solid solutions can tailor the properties of MAX phase coatings [18]. In fact, as a widely used strengthening strategy, solid solution strongly favors the enhancement of mechanical properties for MAX phases. Meng et al. synthesized (Ti$_{1-x}$V$_x$)$_2$AlC ($0 \le x \le 0.2$) and observed enhancements in the Vickers hardness, compressive strength and flexural strength with the increment of V content [19]. Similarly, by

---

substituting Ti with Mo on the M-site, the Vickers hardness, flexural strength and fracture toughness of $(Ti_{1-x}Mo_x)_2AlC$ ($0 \leq x \leq 0.2$) were all improved significantly [20]. Analogous observations were reported for $Ti_3Al_{1-x}Si_xC_2$ [21], $(Cr_{1-x}V_x)_2AlC$ [22,23], $(Ti_{1-x}Zr_x)_3SiC_2$ [24], $(Nb_{0.85}, Zr_{0.15})_4AlC_3$ [25], $(Cr_{2/3}Ti_{1/3})_3AlC_2$ [26] etc. However, certain solid solutions, such as (Ti, Nb)$_2$AlC [27], exhibited a lack of solid solution strengthening effect because its hardness only ranged between its end members Ti_2AlC and Nb_2AlC. In recent attempts for coating technology, solid solution strengthening was achieved in (Cr, V)$_2$AlC coatings by hybrid arc/magnetron sputtering deposition [28].

Solid solution strengthening arises from the lattice distortion induced by the size variance of substituent atoms. A larger variance between substituent and host atoms results in greater lattice distortion and generates more significant strengthening effect, which also applies in MAX phases [29]. Therefore, it is reasonable to infer that the incorporation of larger atoms into Ti_2AlC matrices is a potent strengthening means. Among the diverse M-site elements of 211 phases, Zr has a significantly larger atomic radius than Ti, allowing the possibility for solid solution of Zr in Ti_2AlC to generate the remarkable strengthening. Since both Zr and Ti belong to the same B group, it could be quite feasible to form substitutional solid solution. Additionally, potential radiation resistance due to low neutron capture cross section of Zr is also considered. These expectations provide promising applications for (Ti, Zr)$_2$AlC solid solution coatings as a protective strategy for components used in harsh environment.

Due to the instability of Zr-based MAX phases compared with their competing phases, their synthesis is an enormous challenge [30]. Previous studies on Ti-Zr-Al-C MAX phase system primarily focused on bulk materials, and most of these MAX phases were 312 phases with the existence of secondary phases such as carbides and intermetallics [31–34]. Hadi et al. synthesized a series of solid solutions $(Zr_{3-x}Ti_x)AlC_2$ and investigated their mechanical and thermodynamic properties through theoretical calculation [34,35]. Recently, Azina et al. synthesized (Ti, Zr)$_2$AlC thin films on Al_2O_3 substrates by magnetron sputtering from a compound target with a deposition temperature of 900 °C which was required to form MAX phases [36]. Such a high temperature is unsuitable for temperature-sensitive metal substrates like stainless steel and titanium alloy. Two-step method and high power impulse magnetron sputtering (HiPIMS) have been proven as two efficient methods to lower the formation temperature of MAX phases [37–39]. Compared with the traditional high-temperature deposition in the one-step method, the two-step method means low-temperature deposition followed by extra annealing. HiPIMS technology utilizes pulse discharge with a low duty ratio to generate extremely high peak power density than direct current magnetron sputtering (DCMS) at the same average power. In this regard, both two-step process and HiPIMS yield sufficient energy for atoms or ions to diffuse, which is necessary for the transformation into crystalline MAX phases. Moreover, considering the multi-target convenience for sputtering, it is plausible to first deposit a pristine Ti-Zr-Al-C coating and then fabricate a (Ti, Zr)$_2$AlC MAX phase coating using this specific two-step method.

In this work, we fabricated a substitutional solid solution of Zr in Ti_2AlC coating using HiPIMS technology with multi-target sputtering sources followed by annealing in a vacuum. Since a high Zr content can generate Zr-containing secondary phases [36], a relatively low Zr concentration of approximately 5 % was incorporated into Ti_2AlC to obtain high-purity MAX phases. High-purity Ti_2AlC MAX phase coatings without Zr were also synthesized using the same process for comparison. The dependence of the mechanical properties of coatings on the solid solution of a small amount of Zr on the M-site in Ti_2AlC was investigated. The strengthening effect was discussed in terms of the microstructural evolution induced by Zr solid solution.

2. Materials and methods

2.1. Coatings preparation

Ti-Zr-Al-C coatings were deposited in a home-made hybrid HiPIMS/DCMS system with multi-target sputtering sources, consisting of a TiAl alloy target (Ti:Al = 1:1 at.%, size of Φ50.8 mm × 5 mm, purity of 99.9 %), a graphite target (size of Φ50.8 mm × 5 mm, purity of 99.999 %) and a Zirconium target (size of Φ50.8 mm × 5 mm, purity of 99.99 %). The three targets were arranged confocally at a distance of 80 mm from the substrates in the vertical direction, as illustrated in Fig. 1. Prior to deposition, the chamber was evacuated to a base pressure of 5×10^{-4} Pa, and the sample holder was heated to 200 °C. The substrates were etched in Ar^+ plasma at 2 Pa for 30 min using a pulsed bias of −400 V with a frequency of 150 kHz and a duty ratio of 60 % to remove contaminants and oxides from the substrate surface. During deposition, the TiAl target was operated in HiPIMS, while the C target and the Zr target were operated in DCMS in view of the low ionization rate of C and the requirement for a lower Zr content in the coatings. Specifically, a $TiAl_x$ interlayer with a thickness of approximately 0.2 μm was pre-deposited on the substrates to enhance coating-substrate adhesion. Thereafter, Ti-Zr-Al-C coatings with a thickness of about 3 μm were obtained using three-target co-sputtering. Throughout the deposition process, the sample holder temperature was maintained at 200 °C. The specific deposition parameters are detailed in Table 1. For Ti-Al-C coatings, the same process was followed, except for a higher power applied to the C target and the absence of the Zr target. All the depositions were carried out on Ti-6Al-4V substrates.

Subsequently, as-deposited Ti-Zr-Al-C and Ti-Al-C coatings were annealed in a vacuum using a rapid thermal process furnace (RTP-S304) to crystallize into MAX phases. To minimize oxidation of the coatings during annealing, the furnace was evacuated to below 3×10^{-4} Pa before initiating heating. The samples were then heated to 750 °C and held at that temperature for 90 min. Subsequently, the samples were cooled to 300 °C at a rate of 7.5 °C/min and then naturally cooled to ambient temperature in the furnace.

2.2. Structure and composition characterization

The phase compositions of the as-deposited and annealed coatings were investigated by X-ray diffraction (XRD; Brucker D8 Discover) in Bragg-Brentano geometry, using Cu Kα radiation, over a 2θ scanning range of 10–90° with a step size of 0.02°. Rietveld refinements of the diffraction patterns were specially carried out with the Bruker TOPAS software. The surface morphology and chemical compositions of the coatings were tested using field emission scanning electron microscope (SEM; FEI Quanta FEG 250), equipped with an X-ray energy dispersive spectrometer (EDS; Oxford Instruments). To clearly identify the changes occurred in the coatings, the atomic force microscope (AFM; Veeco Dimension 3100) with a scanning area of 5 μm × 5 μm and the transmission electron microscope (TEM; Thermo Fisher Talos F200X) were comprehensively employed to address the surface roughness and microstructure evolution due to solid solution of Zr. The cross-sectional lamella samples used for TEM characterization were prepared by focused ion beam (FIB; Thermo Fisher Helios G4 CX).

2.3. Mechanical property tests

The residual stresses of crystalline coatings after annealing were measured by two-dimensional X-ray diffractometer (Brucker D8 Discover) using $\sin^2\psi$ method with a ψ range from 0° to 60°. For each sample, the diffraction peak near 60° corresponding to (110) crystal face of Ti_2AlC was especially selected for stress calculation because of its high-intensity for such a single diffraction peak without overlapping other peaks. After measuring the two components along the length and width direction of the substrates, the average was calculated as the
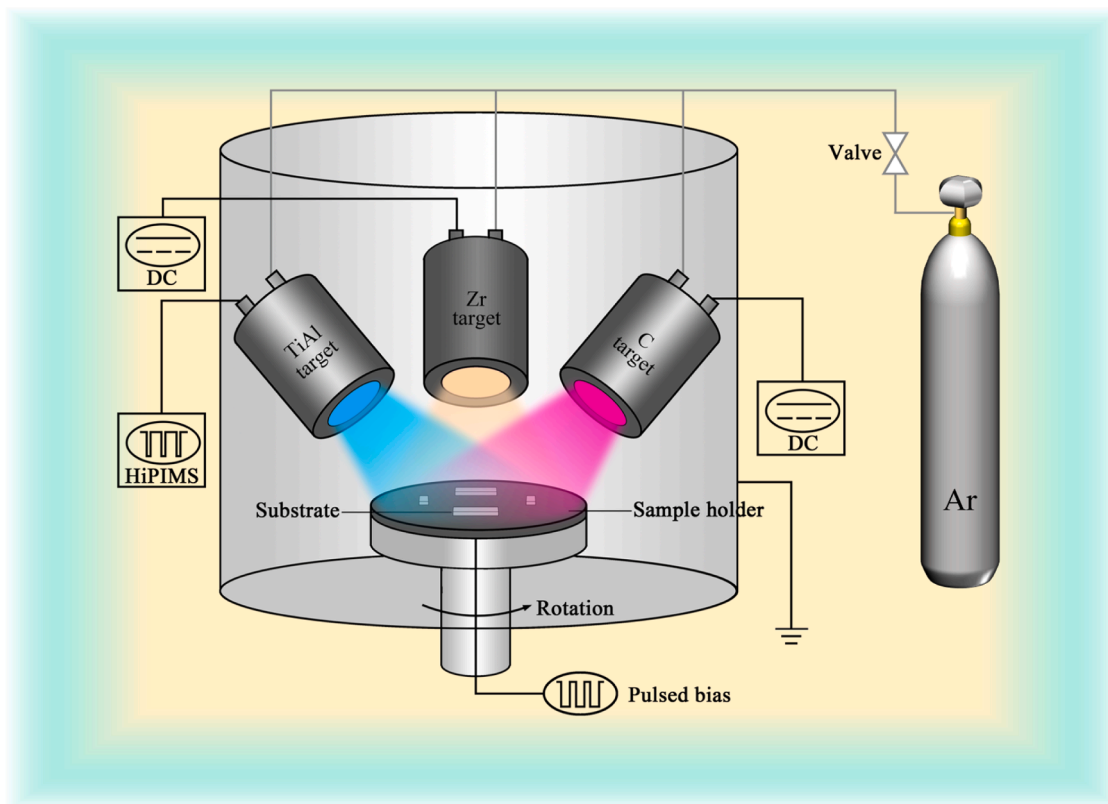
Fig. 1. Schematic diagrams of the multi-target magnetron sputtering system.

Table 1
Deposition parameters of coatings.

Target coatings	Ar pressure (Pa)	Bias (V)	TiAl target (HiPIMS)			C target (DCMS)	Zr target (DCMS)
			Power (W)	Pulse width (μs)	duty ratio (%)	Power (W)	Power (W)
TiAl$_x$ interlayer	0.7	−70	150	50	5	—	—
Ti-Zr-Al-C						50	3
Ti-Al-C						65	—

residual stress of the coatings [40].

The hardness (H) and elastic modulus (E) of the annealed coatings were measured using an MTS G200 nano-indenter with a Berkovich diamond indenter in continuous stiffness measurements (CSM) mode. The maximum penetration depth of the indenter was set about 600 nm and the values of hardness and elastic modulus were determined at the penetration depth of 300 nm, which is only about 10 % of the coating thickness. Such handling was proposed to avoid the influence from the substrate. Each sample was tested with six positions for the average value.

The plasticity and toughness of the annealed coatings was evaluated using a Bruker Hysitron TI980 nano-indenter with a cube-corner diamond indenter, which has an included angle of 90°, significantly sharper than a Berkovich indenter (142.3°). The applied sharper indenter can produce higher stress with a given load, favoring the generation of radial cracks at a very small load [41]. Load-controlled nano-indentation were performed at a maximum load of 10 mN. The three-dimensional profiles of the residual indentations were *in-situ* scanning imaged with the indenter in the contacting mode immediately after an indentation test. The morphology of indentations were specially characterized by SEM. Each sample was tested three times to ensure high duplicability.

3. Results and discussion

3.1. Phase structure and chemical composition

Fig. 2 shows the XRD patterns of the as-deposited and annealed coatings for comparison. All the patterns contained the diffraction peaks arising from Ti-6Al-4V substrates due to the penetration depth of X-rays beyond the coating thickness. Note that in Fig. 2a, a relatively sharp peak at about 39° appeared in both XRD patterns of the as-deposited Ti-Al-C and Ti-Zr-Al-C coatings, which could be ascribed to the presence of TiAl$_x$ intermetallics [42]. This implied that the as-deposited coatings prepared by HiPIMS technique were partially crystalline because of the benefits from high ionization and the incident energy of discharged plasma. Compared with the completely amorphous as-deposited coatings prepared by traditional DCMS as reported previously [42–44], such partially crystalline as-deposited coatings contained intermediate phases in the formation of Ti$_2$AlC, indicating easier synthesis of Ti$_2$AlC coatings using HiPIMS technique. In addition, TiC$_x$ phase was identified by the three board peaks at 37°, 43° and 62°, which is also an intermediate phase besides TiAl$_x$ in the formation of Ti$_2$AlC [37,45–47]. Interestingly, these peaks obviously shifted upwards compared with those of normal TiC$_x$ phases, which could be attributed to metastable solid solution of Al in TiC$_x$ [48,49]. Since Al occupied partial Ti sites in TiC$_x$, the solid solution (Ti, Al)C$_x$ formed instead of TiC$_x$. Consequently,
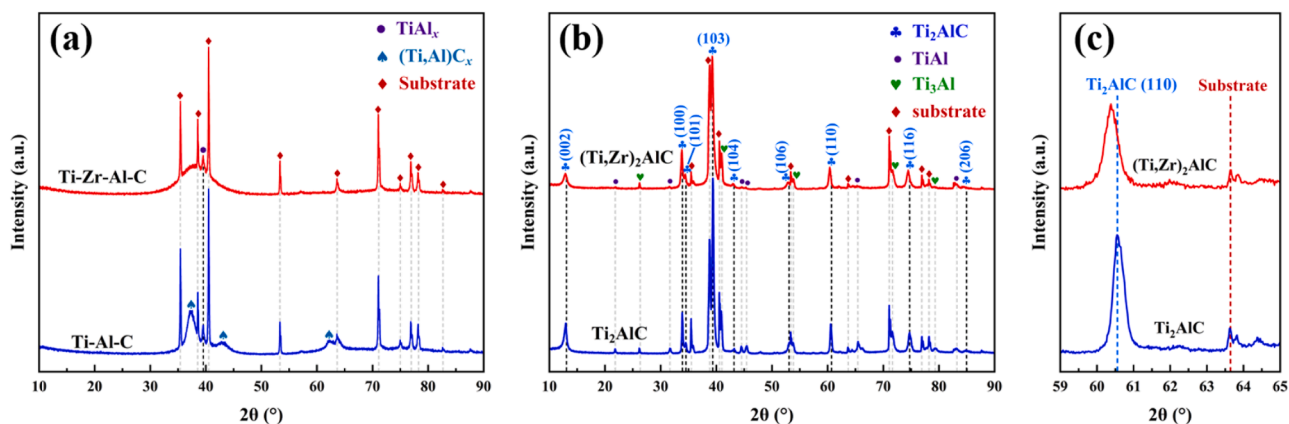
Fig. 2. XRD patterns of (a) the as-deposited coatings and (b) the annealed coatings with (c) partially enlarged view in (b).

smaller Al atoms decreased the interplanar spacing and shifted peaks toward higher angles. However, no visible peak of $(Ti, Al)C_x$ appeared in the pattern of the Ti-Zr-Al-C coating, but instead, a broad diffraction signal between $30°$ and $45°$ corresponding to amorphous state was observed, which contrasted with the absence of an amorphous hump in the pattern of as-deposited Ti-Al-C coating. This observation suggests that the incorporation of Zr into Ti-Al-C coating impeded the crystallization.

After annealing at 750 °C for 90 min, crystalline Ti_2AlC MAX phase was presented in both coatings, identified by the PDF card #04-001-6560 (Fig. 2b). Additionally, although extra TiAl and Ti_3Al phases were identified also by the PDF card #04-006-6741 and #04-004-2732, only a small fraction of TiAl existed in MAX phase layer according to TEM analysis later. Therefore, the observation of TiAl and Ti_3Al in diffraction patterns might arise from interlayers or diffusion layers. Furthermore, Zr-containing intermetallic or carbide [36] was not detected in the coating within the limitation of XRD resolution. The partially enlarged view of the diffraction patterns between $59°$ and $65°$ (Fig. 2c) reveals a downward shift in the peak of Ti_2AlC (110) at $60.5°$ with the addition of Zr, while no shift was observed in the peak of the substrate at $63.6°$. This demonstrates that Zr dissolved into the lattice of Ti_2AlC after annealing, resulting in the formation of $(Ti, Zr)_2AlC$ solid solution. It is worth noting that $(Ti, Zr)_2AlC$ had lower peak intensity and greater full width at half maximum, indicating the possibility for smaller grains and lower crystallinity of $(Ti, Zr)_2AlC$ than Ti_2AlC.

Rietveld refinement was performed to further quantitatively investigate the changes in the lattice parameters of the MAX phases in regard to the solid solution of Zr. The aforementioned three phases, assigned to

Ti_2AlC, TiAl, Ti_3Al, along with the Ti substrate phase (PDF card #04-002-5207), were used as initial crystal structure models. The refinement results were deemed reliable with R_{wp} controlled below 15 % through repeated operation cycles. The refinement results (Fig. 3) suggest that Zr occupied partial sites of Ti in Ti_2AlC with the site occupancy of Zr around 0.1. Therefore, it can be concluded that the MAX phase in the annealed Ti-Zr-Al-C coating was identified as $(Ti_{0.9}Zr_{0.1})_2AlC$. Table 2 presents the details of the lattice parameters of comparative Ti_2AlC and $(Ti_{0.9}Zr_{0.1})_2AlC$ extracted from the refinement results. Clearly, the lattice parameters a and c were 3.058 Å and 13.675 Å for Ti_2AlC, respectively, while they increased to 3.068 Å and 13.709 Å for $(Ti_{0.9}Zr_{0.1})_2AlC$. The ratio of c to a was the same for both Ti_2AlC and $(Ti_{0.9}Zr_{0.1})_2AlC$, demonstrating a homogeneous lattice expansion in all directions. Table 3 listed the d-spacings and 2θ angles of the diffraction peaks for both Ti_2AlC and $(Ti_{0.9}Zr_{0.1})_2AlC$ obtained from the Rietveld refinement.

Table 4 summarized the chemical compositions of the as-deposited and annealed coatings. For the Ti-Al-C coating, the atomic ratio of Ti: Al was about 2:1.75, deviating from the atomic ratio of 1:1 in the sputtered TiAl target, which could be associated with the vaporization and re-sputtering of Al caused by ion bombardment. Moreover, the

Table 2

Lattice parameters of Ti_2AlC and $(Ti_{0.9}Zr_{0.1})_2AlC$.

Phase	a (Å)	c (Å)	c/a	R_{wp} (%)
Ti_2AlC	3.058	13.675	4.47	11.7
$(Ti_{0.9}Zr_{0.1})_2AlC$	3.068	13.709	4.47	9.5
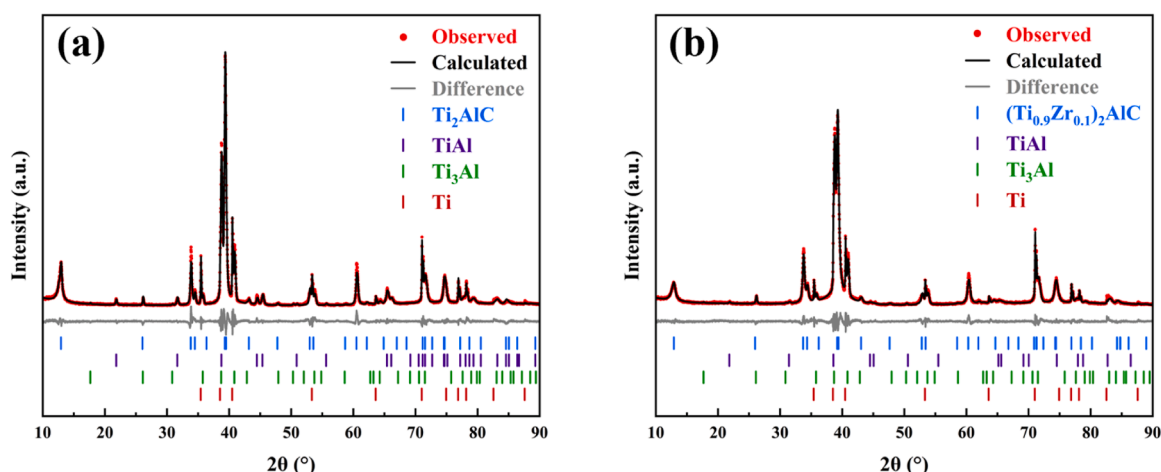
Fig. 3. Rietveld refinement diagrams of the annealed (a) Ti_2AlC coating and (b) $(Ti, Zr)_2AlC$ coating.

Table 3
The d-spacings and 2θ angles of the diffraction peaks of Ti$_2$AlC and (Ti$_{0.9}$Zr$_{0.1}$)$_2$AlC.

h k l	Ti$_2$AlC		(Ti$_{0.9}$Zr$_{0.1}$)$_2$AlC	
	2θ (°)	d (Å)	2θ (°)	d (Å)
0 0 2	12.94	6.837	12.90	6.855
0 0 4	26.04	3.419	25.98	3.427
1 0 0	33.82	2.648	33.71	2.657
1 0 1	34.47	2.600	34.35	2.608
1 0 3	39.32	2.290	39.19	2.297
0 0 6	39.51	2.279	39.40	2.285
1 0 4	43.18	2.093	43.04	2.100
1 0 5	47.77	1.902	47.62	1.908
1 0 6	52.97	1.727	52.80	1.732
1 0 7	58.68	1.572	58.50	1.576
1 1 0	60.51	1.529	60.28	1.534
1 1 2	62.17	1.492	61.94	1.497
1 0 8	64.88	1.436	64.67	1.440
2 0 0	71.16	1.324	70.88	1.328
1 0 9	71.54	1.318	71.26	1.322
2 0 1	71.54	1.318	71.31	1.321
2 0 3	74.58	1.271	74.29	1.276
1 1 6	74.71	1.270	74.43	1.274
2 0 4	77.21	1.235	76.90	1.239
2 0 6	84.58	1.145	84.24	1.148
1 1 8	85.06	1.140	84.79	1.142

Table 4
Chemical compositions of coatings.

Coating	Ti (at.%)	Zr (at.%)	Al (at.%)	C (at.%)
Ti-Al-C	41.2 ± 0.5	—	36.0 ± 0.2	22.8 ± 0.3
Ti$_2$AlC	50.0 ± 0.3	—	26.1 ± 0.3	23.9 ± 0.1
Ti-Zr-Al-C	39.3 ± 0.1	4.9 ± 0.1	32.0 ± 0.1	23.8 ± 0.1
(Ti$_{0.9}$Zr$_{0.1}$)$_2$AlC	43.3 ± 0.2	5.3 ± 0.1	25.7 ± 0.1	25.7 ± 0.3

incorporation of heavy Zr atoms amplified this phenomenon because of the stronger re-sputtering effect, leading to a larger atomic ratio of Ti:Al at 2:1.63 and lower Al content in the Ti-Zr-Al-C coating. It is worth noting that the C content of two as-deposited coatings was similar, even though the power of the C target for the Ti-Zr-Al-C coating was considerably lower than that for the Ti-Al-C coating. This indicates that the addition of Zr sputtering increased the deposition rate of C, which was the key factor in choosing a lower power for the C target in Ti-Zr-C deposition process. After annealing, the Al contents significantly decreased in both coatings because of the high vapor pressure of Al. In this regard, the excess Al in the as-deposited coatings could contribute to the formation of Ti$_2$AlC MAX phase. Consequently, both annealed coatings showed the similar decrease of Al content. The atomic ratio of Zr/Zr+Ti in Ti-Zr-Al-C coating was 0.11 and remained the same value after annealing, implying no loss of Ti and Zr during annealing. This ratio was consistent with the result of the aforementioned Rietveld refinement, suggesting that most of the added Zr dissolved into Ti$_2$AlC matrix.

3.2. Surface morphology and microstructure

Fig. 4 displays representative SEM and AFM micrographs of the Ti$_2$AlC and (Ti$_{0.9}$Zr$_{0.1}$)$_2$AlC coatings for comparison. The dense and crack-free morphology appeared on the surface of both coatings (Fig. 4a and d). Furthermore, the high-magnification image (Fig. 4b) exhibits that equiaxed granular agglomerations were closely packed on the surface of the Ti$_2$AlC coating, generating a cauliflower-like structure, which was typical of PVD-deposited coatings at a low growth temperature [50]. Although the (Ti$_{0.9}$Zr$_{0.1}$)$_2$AlC coating exhibited a similar packed agglomeration surface, the agglomeration size was significantly smaller than that of the Ti$_2$AlC coating, probably due to the increase in nucleation sites and the decrease in agglomeration growth rate promoted by Zr incorporation. Such surface characteristics might arise from Stranski-Krastanov (SK) growth mode [51], also empirically known as
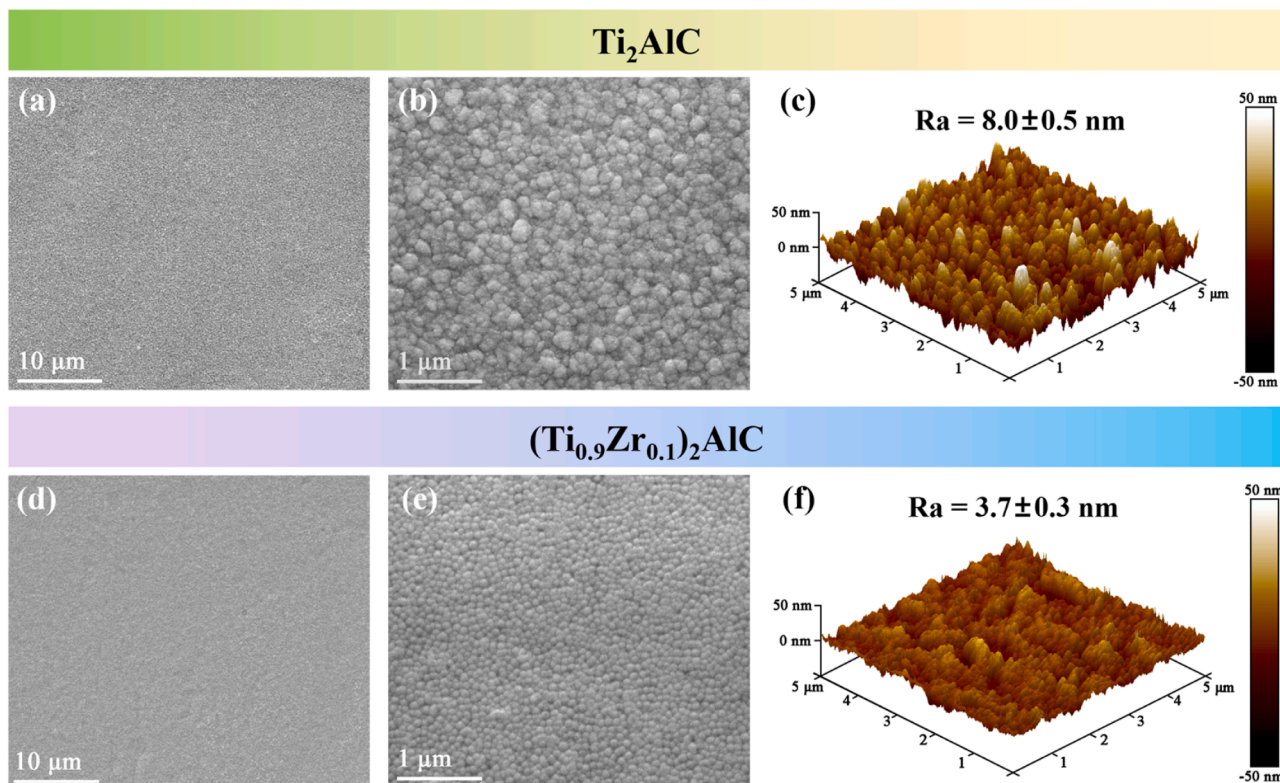
Fig. 4. SEM micrographs and AFM topography maps of (a~c) Ti$_2$AlC coating and (d~f) (Ti$_{0.9}$Zr$_{0.1}$)$_2$AlC coating.

layer-island growth. The island-relevant structure would emerge to reduce the growth stress when the coating thickness exceeded a critical value, which subsequently led to the coalescence of these islands into the close-packed granular agglomerations during growth process [52]. On the one hand, as solute atoms, Zr could serve as nucleation sites to promote nucleation and produce more islands. On the other hand, larger and heavier Zr atoms could impede the kinetic diffusion of other atoms, which would be detrimental to the growth and coalescence process. Evidence for this was the emergence of the $(Ti, Al)C_x$ phase in the Ti-Al-C coating, which was absent in the Ti-Zr-Al-C coating. As a result, the $(Ti_{0.9}Zr_{0.1})_2AlC$ coating exhibited smaller granular agglomerations and a smoother surface morphology, which was further evidenced by the smaller surface roughness as illustrated in Fig. 4c and 4f.

In order to identify the crystalline structure of annealed coatings, Fig. 5 shows comprehensive TEM micrographs and cross-sectional microstructures of the Ti$_2$AlC coating. The bright-field image (Fig. 5a) revealed that the Ti$_2$AlC coating displays a highly dense microstructure throughout the thickness, where no obvious voids, holes or cracks were visible within the coating, interlayer and interface. Combined with the dark-field image (Fig. 5b), lath-shaped crystalline grains with larger sizes along the direction of basal planes and the equiaxed nanograins with similar sizes in all direction were present. Fig. 5c shows the distribution of the grain size along the length direction deduced from the dark-field image, from which the average grain size was estimated to be about 84 nm. The average grain size along the width direction of the grains was estimated to be around 37 nm. The selected-area electron diffraction (SAED) patterns obtained from the two areas marked in Fig. 5a are illustrated in Fig. 5d. Two diffraction patterns were spliced into one figure, and the color of the pattern at Position A was reversed for convenient comparison. The area near the coating surface (Position A) only revealed the diffraction signals from Ti$_2$AlC phase, while the area closer to the interlayer (Position B) demonstrated the strong signals from Ti$_2$AlC phase and weak signals from TiAl phase. This observation

confirms the successful synthesis of high-purity Ti$_2$AlC coating along with a small amount of TiAl intermetallic. Fig. 5e shows higher-magnification bright-field images of the two areas A and B. The circled zone was further specified by high-resolution TEM (HRTEM), as illustrated in Fig. 5f, with an enlarged view of the nanograin in Fig. 5g. When the incident electron beam was parallel to $[11\bar{2}0]$ zone, a typical nano-laminated structure of MAX phase was characterized, where one bright Al layer was tightly sandwiched by two dark Ti layers. Moreover, Fig. 5h displays the SAED pattern within one Ti$_2$AlC nanograin in $[11\bar{2}0]$ direction. The lattice parameter of c measured from HRTEM image was approximately 1.36 nm, which was in accordance with that of Ti$_2$AlC MAX phase.

For comparison, Fig. 6 shows the TEM images of $(Ti_{0.9}Zr_{0.1})_2AlC$ coating. The entire coating was distinctly dense, hole-less and crack-free (Fig. 6a). Unlike the mixed grain characteristics in the Ti$_2$AlC coating, the $(Ti_{0.9}Zr_{0.1})_2AlC$ coating was dominated by equiaxed grains (Fig. 6b). The average grain size was estimated to be about 20 nm (Fig. 6c), which was significantly smaller than 84 nm and 37 nm of the Ti$_2$AlC coating. The grain refinement could be ascribed to two factors. First, with the introduction of Zr into the Ti$_2$AlC matrix, the nucleation sites increased significantly. Second, the atomic diffusion and grain boundary migration were remarkably impeded by Zr. However, like the Ti$_2$AlC coating, the area near the coating surface was dominated by high-purity $(Ti_{0.9}Zr_{0.1})_2AlC$ MAX phase, while the area closer to the interlayer demonstrated a mixture of dominant MAX phase and minor TiAl intermetallic (Fig. 6d). An emblematic structure of one bright layer sandwiched between two dark layers in MAX phase was evidenced by HRTEM images (Fig. 6f and g) of the grain circled in Fig. 6e. Corresponding fast Fourier transform (FFT) image (Fig. 6h) shows typical spots of MAX phases. The c lattice parameter was measured to be about 1.37 nm, slightly larger than that of Ti$_2$AlC, proving the presence of (Ti, Zr)$_2$AlC solid solution. In order to address the elemental distribution in
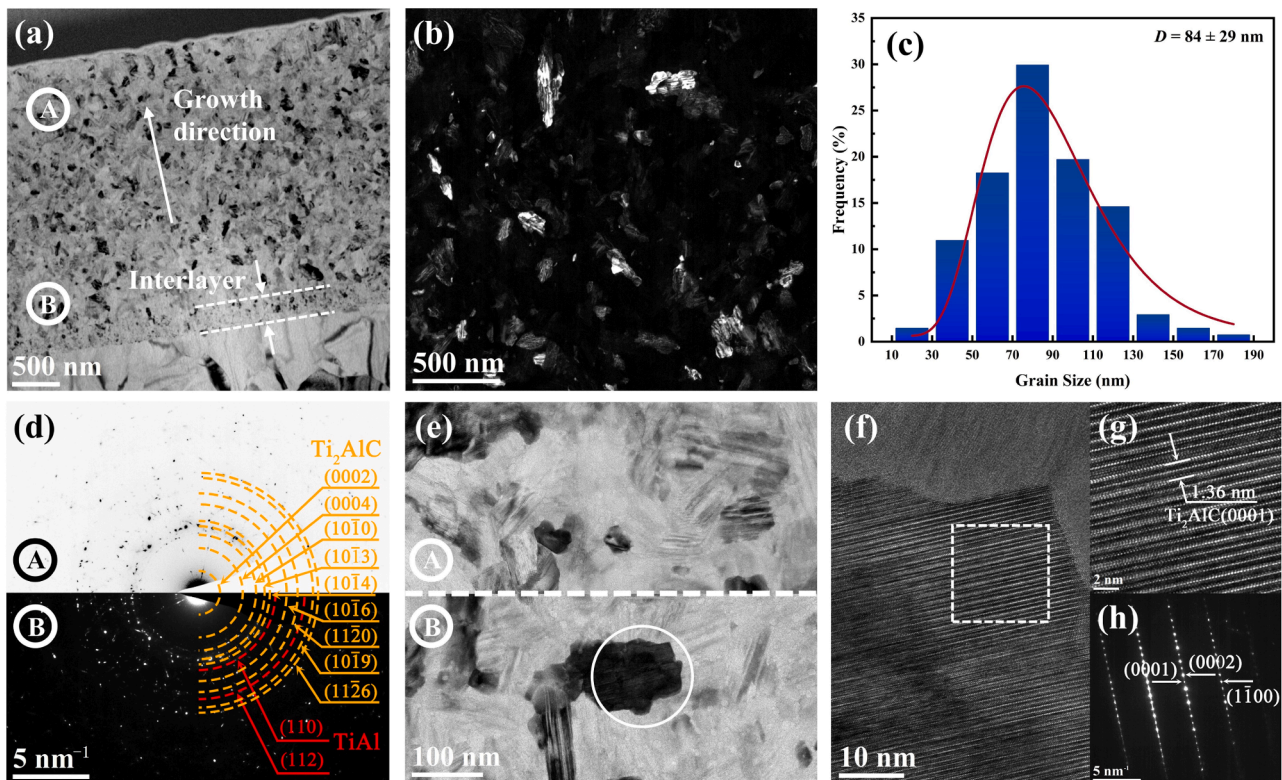
Fig. 5. TEM micrographs of the cross section of Ti$_2$AlC coating. (a) Bright-field image of the overall coating. (b) Dark-field image. (c) The grain size distribution deduced from (b). (d) SAED patterns from the two areas marked in (a). (e) Bright-field images at a high magnification from the areas marked in (a). (f) HRTEM images from the area circled in (e). (g) Enlarged view of the region indicated by the dashed box in (f). (h) SAED pattern from the grain circled in (e).
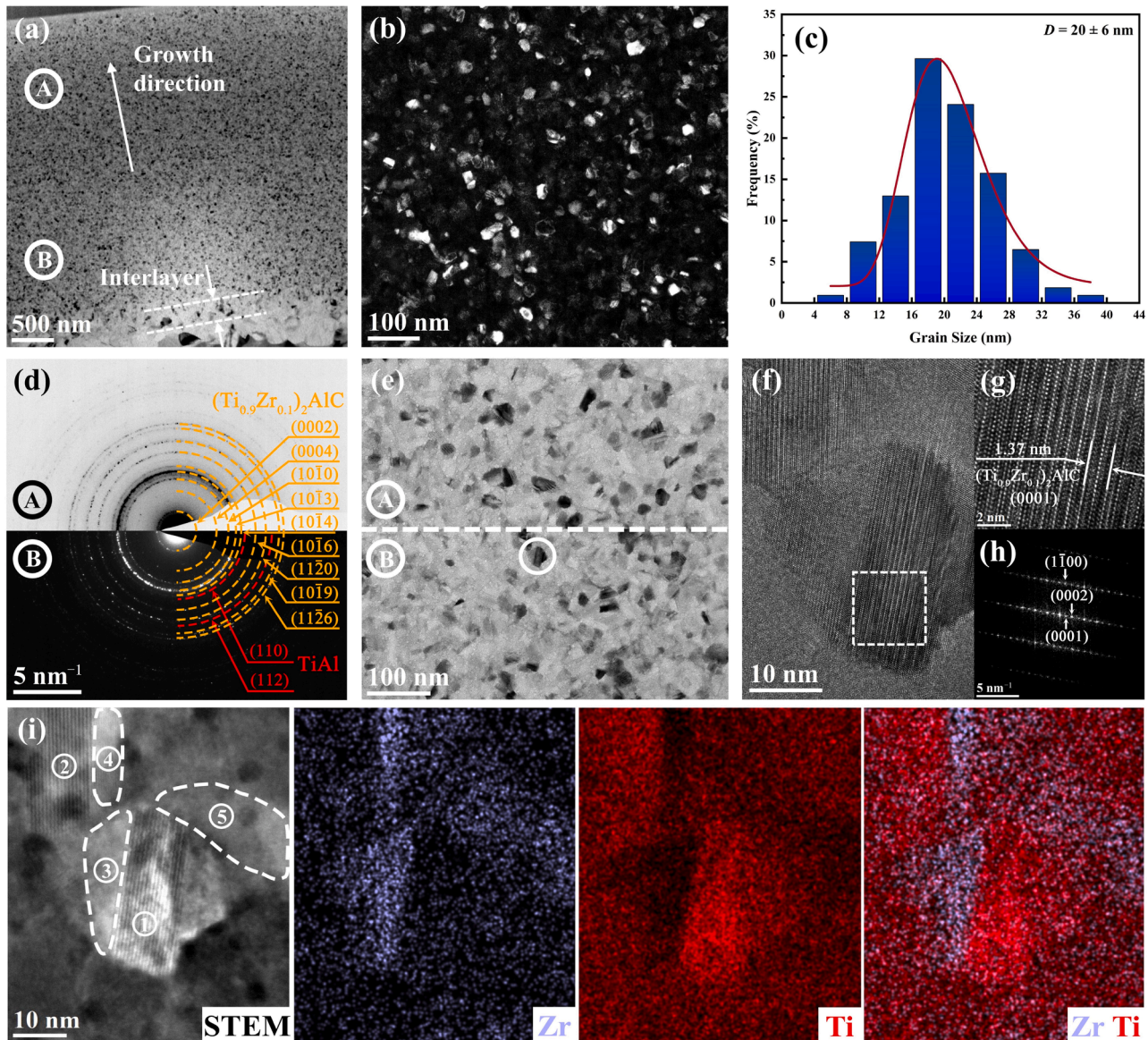
Fig. 6. TEM micrographs of the cross section of $(Ti_{0.9}Zr_{0.1})_2AlC$ coating. (a) Bright-field image of the overall coating. (b) Dark-field image. (c) The grain size distribution deduced from (b). (d) SAED patterns from the two areas marked in (a). (e) Bright-field images at a high magnification from the areas marked in (a). (f) HRTEM images from the area circled in (e). (g) Enlarged view and (h) the corresponding FFT image of the region indicated by a dashed box in (f). (i) STEM micrograph with corresponding Ti and Zr EDS mappings.

the $(Ti_{0.9}Zr_{0.1})_2AlC$ coating, Fig. 6i shows the scanning TEM (STEM) image and the corresponding EDS mappings of the area shown in Fig. 6f. Clearly, the Zr was enriched next to MAX phase grains, which was circled with dashed lines in the STEM image. The same areas were remarkably poor in Ti. These Zr-rich intergranular phases could impede grain growth, resulting in refined grains. To further characterize the segregation behaviors of Zr, a semiquantitative composition analysis for the five positions marked in Fig. 6i were performed using EDS and the results are listed in Table 5 [36,53]. Position 1 and 2 were located in

MAX phase grains with a nano-laminated structure, while Position 3, 4 and 5 were located in Zr-rich intergranular phases. There was a slight difference in the Zr content at the two positions in MAX phases. $Zr/(Ti+Zr)$ was slightly lower than 0.1 at Position 1 and slightly higher than 0.1 at Position 2. This suggested a heterogeneous dissolution of Zr (and Ti) in MAX phase grains. The Zr content at the other three positions reached 0.2 or 0.3, which was significantly higher than that in MAX phases, and the corresponding Ti content was quite low. Notably, the Zr content at Position 5 was also different from that at Position 3 and 4. Such micro-segregation was widespread in the coating.

3.3. Mechanical properties

Fig. 7 shows the comparative mechanical properties of Ti_2AlC and $(Ti_{0.9}Zr_{0.1})_2AlC$ coatings by nanoindentation tests. According to the load-depth curves (Fig. 7a), the $(Ti_{0.9}Zr_{0.1})_2AlC$ coating required a larger load to achieve the same penetration depth as the Ti_2AlC coating, indicating a higher hardness for the $(Ti_{0.9}Zr_{0.1})_2AlC$ coating.

Table 5
EDS semiquantitative analyses of the positions in Fig. 6i.

Position	Ti (at.%)	Zr (at.%)	Al (at.%)	C (at.%)	Ti / (Ti + Zr)
1	62.3	5.7	19.3	12.7	0.08
2	58.1	8.0	20.1	13.8	0.12
3	28.9	29.8	30.6	10.7	0.51
4	29.3	33.5	27.7	9.5	0.53
5	38.3	19.9	27.2	14.6	0.34
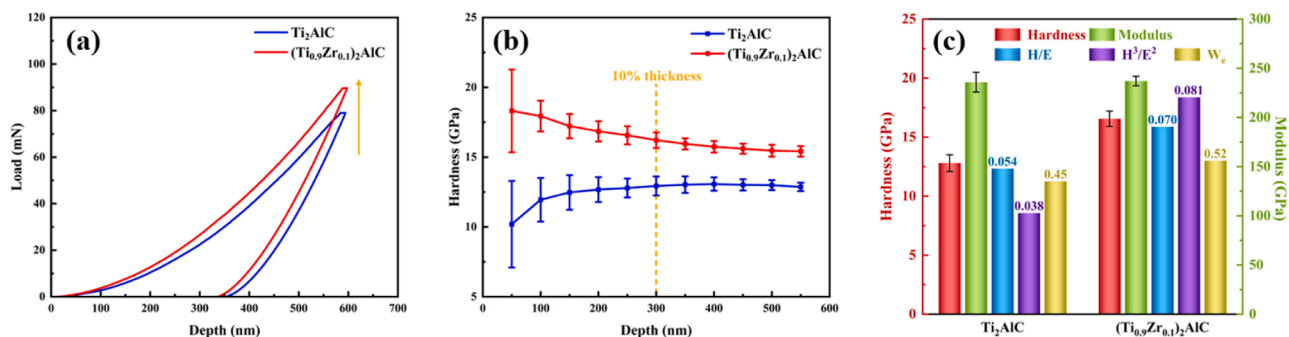
Fig. 7. Nanoindentation with a Berkovich indenter. (a) Load-depth curves. (b) Hardness-depth curves. (c) Mechanical properties of the Ti_2AlC and $(Ti_{0.9}Zr_{0.1})_2AlC$ coatings.

Additionally, the hardness at different depths is displayed in Fig. 7b. In initial loading stage, the hardness gradually increased with increasing depth for the Ti_2AlC coating but decreased for the $(Ti_{0.9}Zr_{0.1})_2AlC$ coating, eventually stabilizing for both coatings. This phenomenon is well known as the indentation size effect in a hard coating combined with a soft substrate [54]. One noticeable result was the severe fluctuation in hardness at shallower depths due to the heterogeneity of grain orientations and surface roughness. Another important observation was the hardness difference between Ti_2AlC and $(Ti_{0.9}Zr_{0.1})_2AlC$ coatings. At a depth of 300 nm, approximately 10 % of the coating thickness, the hardness was about 12.8 GPa for the Ti_2AlC coating and 16.6 GPa for the $(Ti_{0.9}Zr_{0.1})_2AlC$ coating (Fig. 7c). Due to local lattice distortion arising from the atomic size difference between Zr and Ti, the substitution of Zr for Ti generated stress fields that hindered the dislocation motion, yielding solid solution strengthening. Another cause of the increased hardness is related to the grain refinement, especially the formation of Zr-rich intergranular phases. Nevertheless, due to the diminution in valence electron concentration caused by the lattice expansion, the elastic modulus of the $(Ti_{0.9}Zr_{0.1})_2AlC$ declined slightly, which could lead to deteriorated resistance to elastic deformation.

The informative H/E, H^3/E^2 and elastic recovery ratio (W_e) were compared in Fig. 7c. In general, H/E is associated with the limit of elastic behavior, and a large H/E means that larger stress is required to induce obvious plastic deformation [55]. H^3/E^2 is related to yield strength, and plastic deformation is less likely to occur with a large H^3/E^2 [56]. W_e is

the ratio of elastic work to plastic work during elastoplastic deformation, and a large W_e indicates less plastic deformation [57]. For the $(Ti_{0.9}Zr_{0.1})_2AlC$ coating, the value of H/E, H^3/E^2 and W_e were about 0.07, 0.08 and 0.52, respectively. All these three indices were significantly higher than those of the Ti_2AlC coating, suggesting its stronger resistance to plastic deformation.

Considering the importance of plasticity and toughness for practical applications, we further conducted the nanoindentation tests with a sharper cube-corner indenter to penetrate the coatings and produce cracks. Fig. 8 shows the AFM topography maps and corresponding cross-section profiles of the indentations on the Ti_2AlC and $(Ti_{0.9}Zr_{0.1})_2AlC$ coatings. Distinct pile-up phenomena were observed in both coatings. The indentation volume V_{ind}, the pile-up volume V_{pileup} and the ratio of V_{pileup}/V_{ind} were estimated [58]. As shown in Fig. 8e, the pile-up occupied about 40 % of the indentation volume for $(Ti_{0.9}Zr_{0.1})_2AlC$ coating, smaller than 54 % for Ti_2AlC coating. Since these results were evaluated after fully indentation recovery, the ratios of V_{pileup}/V_{ind} could be used to address the actual values. In this regard, the Ti_2AlC coating indeed exhibited larger plasticity to accommodate deformation caused by local pressing. Conversely, the $(Ti_{0.9}Zr_{0.1})_2AlC$ coating revealed a larger resistance to plastic deformation because of the impediment effect of added Zr atoms and strengthened grain boundaries on dislocation motion.

Fig. 9 shows the surface morphology of the indentations. Fine radial cracks formed at the three corners of the indentation on the
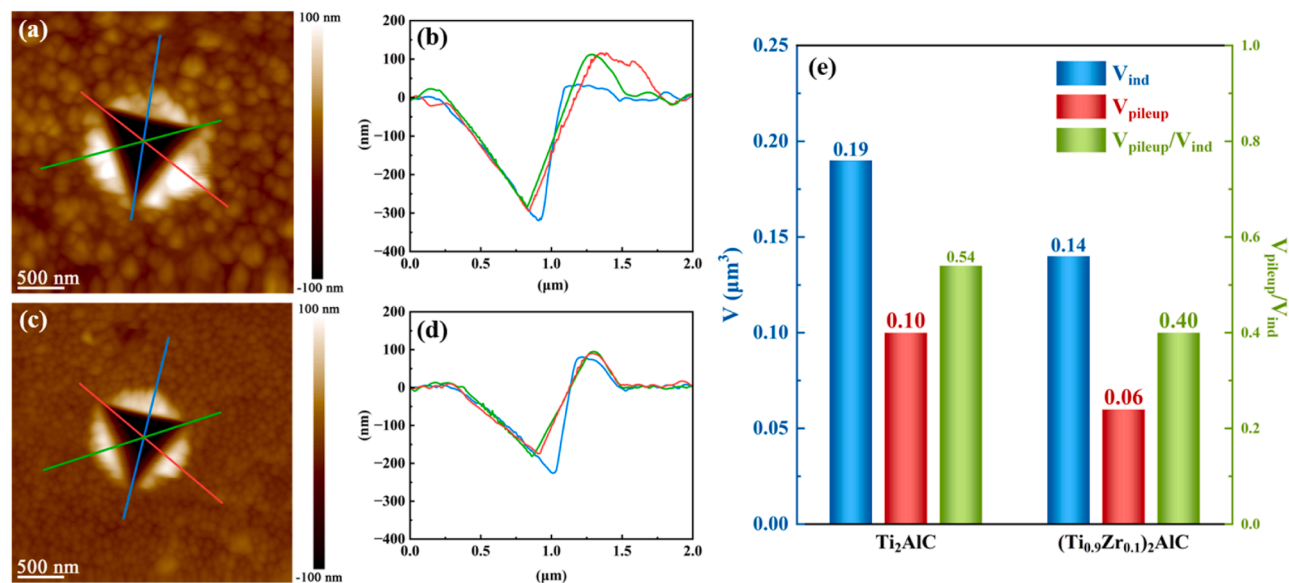
Fig. 8. Nanoindentation with a cube-corner indenter. (a) AFM topography map and (b) section profiles of the indentation on the Ti_2AlC coating. (c) AFM topography map and (d) section profiles of the indentation on the $(Ti_{0.9}Zr_{0.1})_2AlC$ coating. (e) Comparative ratio of pile-up to indentation volume for two coatings.
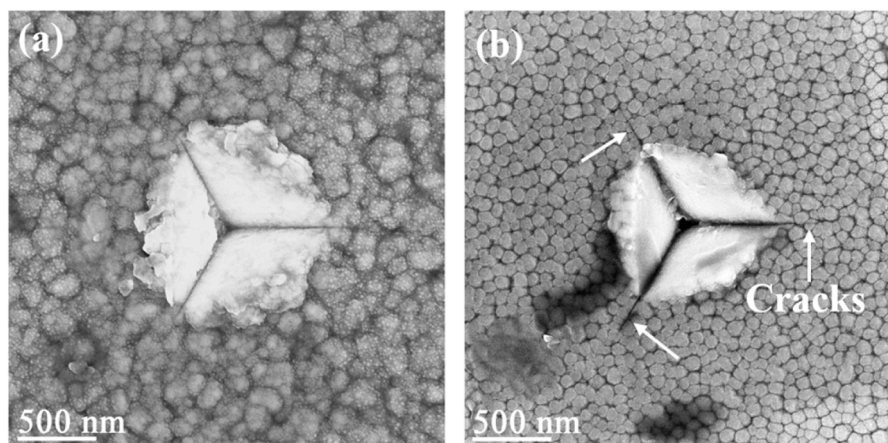
Fig. 9. Surface morphology of the indentation for the (a) Ti$_2$AlC coating and (b) (Ti$_{0.9}$Zr$_{0.1}$)$_2$AlC coating.

(Ti$_{0.9}$Zr$_{0.1}$)$_2$AlC coating, while no cracks emerged on the Ti$_2$AlC coating. It indicates that Zr solid solution led to a lower fracture toughness in the (Ti$_{0.9}$Zr$_{0.1}$)$_2$AlC coating. This plastic deformation behavior can be understood from two aspects. Firstly, the substitutional solid solution of Zr impeded the dislocation motion and the release of the strain energy generated by plastic deformation. This resulted in more strain energy to be stored within the coating as the activation energy for cracking propagation. Similar evidence can be checked from the residual stress of the coatings, which were approximately 17 ± 16 MPa for the Ti$_2$AlC coating and 58 ± 19 MPa for the (Ti$_{0.9}$Zr$_{0.1}$)$_2$AlC coating, based on the results from two-dimensional X-ray diffractometer. Secondly, the fracture failure of MAX phase coating with nanocrystalline microstructure were dominated by intergranular fracture, where grain boundaries served as the preferential crack path [59]. Therefore, Zr-rich intergranular phases could decrease the cohesion of grain boundaries and cause intergranular fracture. In this case, the results of cube-corner indenter test provide a more credible identification of fracture toughness for MAX phase coatings than traditional indicators of H/E and H^3/E^2 obtained by nanoindentation measurements with a Berkovich indenter.

4. Conclusion

In this work, we fabricated high-purity Ti$_2$AlC and (Ti$_{0.9}$Zr$_{0.1}$)$_2$AlC MAX phase coatings on Ti-6Al-4V substrates by a hybrid HiPIMS/DCMS technique with three-target sputtering sources and a subsequent annealing process. The solid solution concentration of Zr was about 5 at. % in the Ti$_2$AlC matrix. Both Ti$_2$AlC and (Ti$_{0.9}$Zr$_{0.1}$)$_2$AlC coatings exhibited surface morphology of closely-packed granular agglomerations. However, the presence of Zr could promote nucleation sites and impede atomic diffusion, resulting in the decrease of surface roughness and refinement of nanocrystalline grains in the (Ti$_{0.9}$Zr$_{0.1}$)$_2$AlC coating. The Ti$_2$AlC coating was a combination of lath-shaped and equiaxed nanograins, while the (Ti$_{0.9}$Zr$_{0.1}$)$_2$AlC coating was almost all refined equiaxed nanograins. The synergistic effect of solid solution strengthening and grain refinement strengthening resulted in a 30 % improvement in the hardness of the (Ti$_{0.9}$Zr$_{0.1}$)$_2$AlC coating from 12.8 GPa to 16.6 GPa, accompanied by improved resistance to plastic deformation. However, the fracture toughness of the (Ti$_{0.9}$Zr$_{0.1}$)$_2$AlC coating slightly declined, which could be attributed to the hardness-toughness trade-off and accelerated intergranular fracture along weaken grain boundaries induced by Zr-rich intergranular phases. These findings not only provide a promising strategy to modify the physiochemical performance of Ti$_2$AlC MAX phase coatings through solution concepts, but also propose an alternative idea to balance hardness and toughness for practical applications.

CRediT authorship contribution statement

Kaihang Wang: Writing – original draft, Visualization, Investigation, Formal analysis, Data curation. **Zhongchang Li:** Validation, Formal analysis. **Yan Zhang:** Validation, Methodology. **Guanshui Ma:** Validation. **Guangxue Zhou:** Funding acquisition. **Peiling Ke:** Funding acquisition. **Zhenyu Wang:** Writing – review & editing, Supervision, Methodology, Funding acquisition. **Aiying Wang:** Writing – review & editing, Supervision, Resources, Project administration, Funding acquisition, Conceptualization.

Declaration of competing interest

The authors declare that they have no known competing financial interests or personal relationships that could have appeared to influence the work reported in this paper.

Data availability

Data will be made available on request.

References

[1] M.W. Barsoum, The M$_{N+1}$AX$_N$ phases: a new class of solids, Prog. Solid State Chem. 28 (2000) 201–281, https://doi.org/10.1016/S0079-6786(00)00006-6.

[2] T. Rackl, D. Johrendt, The MAX phase borides Zr$_2$SB and Hf$_2$SB, Solid State Sci. 106 (2020) 1–6, https://doi.org/10.1016/j.solidstatesciences.2020.106316.

[3] M.A. Hadi, Superconducting phases in a remarkable class of metallic ceramics, J. Phys. Chem. Solids 138 (2020) 109275, https://doi.org/10.1016/j.jpcs.2019.109275.

[4] Q. Zhang, Y. Zhou, X. San, W. Li, Y. Bao, Q. Feng, S. Grasso, C. Hu, Zr$_2$SeB and Hf$_2$SeB: two new MAB phase compounds with the Cr$_2$AlC-type MAX phase (211 phase) crystal structures, J. Adv. Ceram. 11 (2022) 1764–1776, https://doi.org/10.1007/s40145-022-0646-7.

[5] Z. Li, E. Wu, K. Chen, X. Wang, G.X. Chen, L. Miao, Y. Zhang, Y. Song, S. Du, Z. Chai, Q. Huang, Chalcogenide MAX phases Zr$_2$Se(B$_{1-x}$Se$_x$) (x=0–0.97) and their conduction behaviors, Acta Mater. 237 (2022) 118183, https://doi.org/10.1016/j.actamat.2022.118183.

[6] M.A. Hadi, M. Akhter, M.S. Ahasan, I. Ahmed, M.A. Kashem, Realization of diversity in physical properties of Zr$_2$Se(B$_{1-x}$Se$_x$) MAX phases through DFT approach, J. Am. Ceram. Soc. 106 (2023) 6177–6193, https://doi.org/10.1111/jace.19271.

[7] M.A. Hadi, Role of chalcogen atoms as an a-site element on the physical properties of 211 MAX phases in the Hf-A-B system, J. Phys. Chem. C 127 (2023) 23489–23503, https://doi.org/10.1021/acs.jpcc.3c06458.

[8] M. Magnuson, M. Mattesini, Chemical bonding and electronic-structure in MAX phases as viewed by X-ray spectroscopy and density functional theory, Thin Solid Films 621 (2017) 108–130, https://doi.org/10.1016/j.tsf.2016.11.005.

[9] P. Eklund, M. Beckers, U. Jansson, H. Högberg, L. Hultman, The $M_{n+1}AX_n$ phases: materials science and thin-film processing, Thin Solid Films 518 (2010) 1851–1878, https://doi.org/10.1016/j.tsf.2009.07.184.

[10] Z.M. Sun, Progress in research and development on MAX phases: a family of layered ternary compounds, Int. Mater. Rev. 56 (2011) 143–166, https://doi.org/10.1179/1743280410Y.0000000001.

[11] X.H. Wang, Y.C. Zhou, High-temperature oxidation behavior of Ti_2AlC in air, Oxid. Met. 59 (2003) 303–320, https://doi.org/10.1023/A:1023092027697.

[12] X. Wang, Y. Zhou, Oxidation behavior of Ti_3AlC_2 at 1000–1400°C in air, Corros. Sci. 45 (2003) 891–907, https://doi.org/10.1016/S0010-938X(02)00177-4.

[13] Z.J. Lin, M.S. Li, J.Y. Wang, Y.C. Zhou, High-temperature oxidation and hot corrosion of Cr_2AlC, Acta Mater. 55 (2007) 6182–6191, https://doi.org/10.1016/j.actamat.2007.07.024.

[14] S. Li, G. Song, K. Kwakernaak, S. van der Zwaag, W.G. Sloof, Multiple crack healing of a Ti_2AlC ceramic, J. Eur. Ceram. Soc. 32 (2012) 1813–1820, https://doi.org/10.1016/j.jeurceramsoc.2012.01.017.

[15] Z. Wang, G. Ma, Z. Li, H. Ruan, J. Yuan, L. Wang, P. Ke, A. Wang, Corrosion mechanism of Ti_2AlC MAX phase coatings under the synergistic effects of water vapor and solid NaCl at 600 °C, Corros. Sci. 192 (2021) 109788, https://doi.org/10.1016/j.corsci.2021.109788.

[16] M.W. Barsoum, M. Radovic, Elastic and Mechanical Properties of the MAX Phases, Annu. Rev. Mater. Res. 41 (2011) 195–227, https://doi.org/10.1146/annurev-matsci-062910-100448.

[17] J. Gonzalez-Julian, Processing of MAX phases: from synthesis to applications, J. Am. Ceram. Soc. 104 (2021) 659–690, https://doi.org/10.1111/jace.17544.

[18] B.K. Rakhadilov, O.V. Maksakova, D.B. Buitkenov, M.K. Kylyshkanov, D. Pogrebnjak, V.P. Antypenko, Y.V. Konoplianchenko, Structural-phase and tribo-corrosion properties of composite Ti_3SiC_2/TiC MAX-phase coatings: an experimental approach to strengthening by thermal annealing, Appl. Phys. A 128 (2022) 145, https://doi.org/10.1007/s00339-022-05277-7.

[19] F.L. Meng, Y.C. Zhou, J.Y. Wang, Strengthening of Ti_2AlC by substituting Ti with V, Scr. Mater. 53 (2005) 1369–1372, https://doi.org/10.1016/j.scriptamat.2005.08.030.

[20] R. Pan, J. Zhu, Y. Liu, Synthesis, microstructure and properties of $(Ti_{1-x}, Mo_x)_2AlC$ phases, Mater. Sci. Technol. 34 (2018) 1064–1069, https://doi.org/10.1080/02670836.2017.1419614.

[21] H. Gao, R. Benitez, W. Son, R. Arroyave, M. Radovic, Structural, physical and mechanical properties of $Ti_3(Al_{1-x}Si_x)C_2$ solid solution with x=0–1, Mater. Sci. Eng. A 676 (2016) 197–208, https://doi.org/10.1016/j.msea.2016.08.098.

[22] W.B. Tian, Z.M. Sun, H. Hashimoto, Y.L. Du, Synthesis, microstructure and properties of $(Cr_{1-x}V_x)_2AlC$ solid solutions, J. Alloys Compd. 484 (2009) 130–133, https://doi.org/10.1016/j.jallcom.2009.04.111.

[23] J. Zhu, H. Jiang, F. Wang, Q. Ma, Synthesis, microstructure evolution, and mechanical properties of $(Cr_{1-x}V_x)_2AlC$ ceramics by *in situ* hot-pressing method, J. Mater. Res. 29 (2014) 1168–1174, https://doi.org/10.1557/jmr.2014.91.

[24] L. Qu, G. Bei, B. Stelzer, H. Rueß, J.M. Schneider, D. Cao, S. van der Zwaag, W. G. Sloof, Synthesis, crystal structure, microstructure and mechanical properties of $(Ti_{1-x}Zr_x)_3SiC_2$ MAX phase solid solutions, Ceram. Int. 45 (2019) 1400–1408, https://doi.org/10.1016/j.ceramint.2018.10.030.

[25] T. Tytko, D. Tytko, K. Vanmeensel, S. Huang, P.P. Choi, D. Raabe, E.N. Caspi, O. Ozeri, M. to Baben, J.M. Schneider, K. Lambrinou, J. Vleugels, $(Nb_x, Zr_{1-x})_4AlC_3$ MAX phase solid solutions: processing, mechanical properties, and density functional theory calculations, Inorg. Chem. 55 (2016) 5445–5452, https://doi.org/10.1021/acs.inorgchem.6b00484.

[26] Z. Liu, J. Yang, Y. Qian, J. Xu, J. Zuo, M. Li, *In-situ* reaction synthesis and mechanical properties of quaternary MAX phase $(Cr_{2/3}Ti_{1/3})_3AlC_2$, Ceram. Int. 46 (2020) 22854–22860, https://doi.org/10.1016/j.ceramint.2020.06.055.

[27] I. Salama, T. El-Raghy, M. Barsoum, Synthesis and mechanical properties of Nb_2AlC and $(Ti,Nb)_2AlC$, J. Alloys Compd. 347 (2002) 271–278, https://doi.org/10.1016/S0925-8388(02)00756-9.

[28] H. Ruan, Z. Wang, L. Wang, L. Sun, H. Peng, P. Ke, A. Wang, Designed Ti/TiN sub-layers suppressing the crack and erosion of TiAlN coatings, Surf. Coat. Technol. 438 (2022) 128419, https://doi.org/10.1016/j.surfcoat.2022.128419.

[29] Z. Zhang, X. Duan, D. Jia, Y. Zhou, S. van der Zwaag, On the formation mechanisms and properties of MAX phases: a review, J. Eur. Ceram. Soc. 41 (2021) 3851–3878, https://doi.org/10.1016/j.jeurceramsoc.2021.02.002.

[30] A. Poulou, T.A. Mellan, M.W. Finnis, Stability of Zr-Al-C and Ti-Al-C MAX phases: a theoretical study, Phys. Rev. Mater. 5 (2021) 1–19, https://doi.org/10.1103/PhysRevMaterials.5.033608.

[31] D.Y. Kovalev, M.A. Luginina, S.G. Vadchenko, S.V. Konovalikhin, A.E. Sychev, A. S. Shchukin, Synthesis of a new MAX phase in the Ti–Zr–Al–C system, Mendeleev Commun. 27 (2017) 59–60, https://doi.org/10.1016/j.mencom.2017.01.018.

[32] S.V. Konovalikhin, S.A. Guda, D.Y. Kovalev, Composition and structure of $(Zr_{0.37}Ti_{0.63})_3AlC_2$ MAX phase crystals prepared by self-propagating high-temperature synthesis, Inorg. Mater. 54 (2018) 953–956, https://doi.org/10.1134/S0020168518090054.

[33] B. Tunca, T. Lapauw, O.M. Karakulina, M. Batuk, T. Cabioc'h, J. Hadermann, R. Delville, K. Lambrinou, J. Vleugels, Synthesis of MAX phases in the Zr-Ti-Al-C system, Inorg. Chem. 56 (2017) 3489–3498, https://doi.org/10.1021/acs.inorgchem.6b03057.

[34] E. Zapata-Solvas, M.A. Hadi, D. Horlait, D.C. Parfitt, A. Thibaud, A. Chroneos, W. E. Lee, Synthesis and physical properties of $(Zr_{1-x}, Ti_x)_3AlC_2$ MAX phases, J. Am. Ceram. Soc. 100 (2017) 3393–3401, https://doi.org/10.1111/jace.14870.

[35] M.A. Hadi, M. Roknuzzaman, A. Chroneos, S.H. Naqib, A.K.M.A. Islam, R.V. Vovk, K. Ostrikov, Elastic and thermodynamic properties of new $(Zr_{3-x}Ti_x)AlC_2$ MAX-phase solid solutions, Comput. Mater. Sci. 137 (2017) 318–326, https://doi.org/10.1016/j.commatsci.2017.06.007.

[36] C. Azina, B. Tunca, A. Petruhins, B. Xin, M. Yildizhan, P.O.Å. Persson, J. Vleugels, K. Lambrinou, J. Rosen, P. Eklund, Deposition of MAX phase-containing thin films from a $(Ti,Zr)_2AlC$ compound target, Appl. Surf. Sci. 551 (2021) 149370, https://doi.org/10.1016/j.apsusc.2021.149370.

[37] Z. Wang, W. Li, Y. Liu, J. Shuai, P. Ke, A. Wang, Diffusion-controlled intercalation approach to synthesize the Ti_2AlC MAX phase coatings at low temperature of 550 °C, Appl. Surf. Sci. 502 (2020) 144130, https://doi.org/10.1016/j.apsusc.2019.144130.

[38] M. Ougier, A. Michau, F. Schuster, H. Maskrot, M.L. Schlegel, Effects of HiPIMS discharges and annealing on Cr-Al-C thin films, Surf. Coat. Technol. 399 (2020) 126141, https://doi.org/10.1016/j.surfcoat.2020.126141.

[39] Y. Jiang, S. Mráz, J.M. Schneider, Growth of V-Al-C thin films by direct current and high power impulse magnetron sputtering from a powder metallurgical composite target, Thin Solid Films 538 (2013) 1–6, https://doi.org/10.1016/j.tsf.2012.09.021.

[40] Q. Luo, A.H. Jones, High-precision determination of residual stress of polycrystalline coatings using optimised XRD-sin2ψ technique, Surf. Coat. Technol. 205 (2010) 1403–1408, https://doi.org/10.1016/j.surfcoat.2010.07.108.

[41] J. Jang, G.M. Pharr, Influence of indenter angle on cracking in Si and Ge during nanoindentation, Acta Mater. 56 (2008) 4458–4469, https://doi.org/10.1016/j.actamat.2008.05.005.

[42] Z. Li, G. Zhou, Z. Wang, J. Yuan, P. Ke, A. Wang, HiPIMS induced high-purity Ti_3AlC_2 MAX phase coating at low-temperature of 700 °C, J. Eur. Ceram. Soc. 43 (2023) 4673–4683, https://doi.org/10.1016/j.jeurceramsoc.2023.03.059.

[43] J. Yuan, Z. Wang, G. Ma, X. Bai, Y. Li, X. Cheng, P. Ke, A. Wang, MAX phase forming mechanism of M–Al–C (M = Ti, V, Cr) coatings: *in-situ* X-ray diffraction and first-principle calculations, J. Mater. Sci. Technol. 143 (2023) 140–152, https://doi.org/10.1016/j.jmst.2022.09.045.

[44] N. Laska, P.P. Bauer, O. Helle, F. Kreps, Sputtering and characterization of MAX-phase forming Cr–Al–C and Ti–Al–C coatings and their application on γ-based titanium aluminides, Adv. Eng. Mater. 24 (2022) 2100722, https://doi.org/10.1002/adem.202100722.

[45] S. Hashimoto, N. Nishina, K. Hirao, Y. Zhou, H. Hyuga, S. Honda, Y. Iwamoto, Formation mechanism of Ti_2AlC under the self-propagating high-temperature synthesis (SHS) mode, Mater. Res. Bull. 47 (2012) 1164–1168, https://doi.org/10.1016/j.materresbull.2012.02.003.

[46] T. Thomas, C.R. Bowen, Effect of particle size on the formation of Ti_2AlC using combustion synthesis, Ceram. Int. 42 (2016) 4150–4157, https://doi.org/10.1016/j.ceramint.2015.11.088.

[47] A. Abdulkadhim, T. Takahashi, D. Music, F. Munnik, J.M. Schneider, MAX phase formation by intercalation upon annealing of TiC/Al $(0.4 \leqslant x \leqslant 1)$ bilayer thin films, Acta Mater. 59 (2011) 6168–6175, https://doi.org/10.1016/j.actamat.2011.06.029.

[48] O. Wilhelmsson, J.P. Palmquist, T. Nyberg, U. Jansson, Deposition of Ti_2AlC and Ti_3AlC_2 epitaxial films by magnetron sputtering, Appl. Phys. Lett. 85 (2004) 1066–1068, https://doi.org/10.1063/1.1780597.

[49] Y. Li, G. Zhao, Y. Qian, J. Xu, M. Li, Deposition and characterization of phase-pure Ti_2AlC and Ti_3AlC_2 coatings by DC magnetron sputtering with cost-effective targets, Vacuum 153 (2018) 62–69, https://doi.org/10.1016/j.vacuum.2018.04.001.

[50] J.A. Thornton, Influence of apparatus geometry and deposition conditions on the structure and topography of thick sputtered coatings, J. Vac. Sci. Technol. 11 (1974) 666–670, https://doi.org/10.1116/1.1312732.

[51] M. Rashidi, M. Tamizifar, S.M.A. Boutorabi, Influence of deposition temperature on microstructure formation of Ti-Al-C-N ceramic coatings prepared via pulsed-DC PACVD, Surf. Coat. Technol. 407 (2021) 126688, https://doi.org/10.1016/j.surfcoat.2020.126688.

[52] A. Baskaran, P. Smereka, Mechanisms of Stranski-Krastanov growth, J. Appl. Phys. 111 (2012) 044321, https://doi.org/10.1063/1.3679068.

[53] A.D. Pogrebnjak, R.F. Webster, R.D. Tilley, V.V. Buranich, V.I. Ivashchenko, Y. Takeda, K. Oyoshi, R. Sakenova, K. Piotrowska, P. Zukowski, P. Konarski, A. I. Kupchishin, P. Budzynski, Formation of Si-rich interfaces by radiation-induced diffusion and microsegregation in CrN/ZrN nanolayer coating, ACS Appl. Mater. Interfaces 13 (2021) 16928–16938, https://doi.org/10.1021/acsami.0c19451.

[54] G.M. Pharr, E.G. Herbert, Y. Gao, The indentation size effect: a critical examination of experimental observations and mechanistic interpretations, Annu. Rev. Mater. Res. 40 (2010) 271–292, https://doi.org/10.1146/annurev-matsci-070909-104456.

[55] J.A. Greenwood, J.P. Williamson, Contact of nominally flat surfaces, Proc. R. Soc. London. Ser. A 295 (1966) 300–319, https://doi.org/10.1098/rspa.1966.0242.

[56] K.L. Johnson. Contact Mechanics, Cambridge University Press, London, 1985, https://doi.org/10.1017/CBO9781139171731.

[57] M. Liu, Z. Cong, H. Fu, P. Li, Relationships in instrumented indentation by Berkovich indenter, J. Mater. Res. 37 (2022) 4084–4102, https://doi.org/10.1557/s43578-022-00769-x.

[58] D. Giuntini, S. Zhao, T. Krekeler, M. Li, M. Blankenburg, B. Bor, G. Schaan, B. Domènech, M. Müller, I. Scheider, M. Ritter, G.A. Schneider, Defects and plasticity in ultrastrong supercrystalline nanocomposites, Sci. Adv. 7 (2021) 1–11, https://doi.org/10.1126/sciadv.abb6063.

[59] B. Völker, B. Stelzer, S. Mráz, H. Rueß, R. Sahu, C. Kirchlechner, G. Dehm, J. M. Schneider, On the fracture behavior of Cr_2AlC coatings, Mater. Des. 206 (2021) 109757, https://doi.org/10.1016/j.matdes.2021.109757.